International Journal of Computational Methods
Vol. 4, No. 3 (2007) 493–519

World Scientific
www.worldscientific.com

COMPUTATIONAL MODELING OF TURBULENT VELOCITY STRUCTURES FOR AN OPEN CHANNEL FLOW USING KARHUNEN–LOÉVE EXPANSION

R. J. CONNELL* and D. KULASIRI†

Centre for Advanced Computational Solutions (C-fACS)
Lincoln University, PO Box 84, Canterbury, New Zealand
**connelr2@lincoln.ac.nz*
†*kulasird@lincoln.ac.nz*

J. LENNON

PB Water, 100 South Charles ST Baltimore MD 21201 USA
lennonj@pbworld.com

D. F. HILL

Department Civil and Environmental Engineering
Pennsylvania State University, 212 Stackett Building
University Park, PA 16802, USA
dfh2@psu.edu

Received 27 May 2006
Accepted 27 June 2007

This paper develops an analytical two-part covariance kernel from velocity correlations across a two-dimensional (vertical and flow directions) Particle Image Velocimetry (PIV) flow field. This will form the basis of a model of wave action in flood water that includes the underlying turbulence velocity field using Karhunen–Loéve (KL) expansion. The PIV data was from the supercritical flow area immediately upstream of an undular hydraulic jump. This paper derives a one-dimensional solution for the associated integral equations. It also discusses a relationship between the two parts of the kernel and the turbulent production and turbulent dissipation.

Keywords: Flood modeling; proper orthogonal decomposition; covariance kernel.

1. Introduction

The Karhunen–Loéve (KL) expansion has been used to analyze turbulent structures in fluid flow. This technique has several other names including Proper Orthogonal Decomposition (POD) and principal components analysis, and is very similar to singular value decomposition and has also been used to analyze other stochastic

†Corresponding author.

phenomena. This technique, under the name of POD, was first used on a turbulent fluid flow, to assess the flow structure in the boundary layer of a pipe flow by Bakewell and Lumley [1967]. The streamwise velocity component of glycerine flow in a pipe in the wall region ($y^+ < 40$) was decomposed using this technique, [where $y^+ = yu^*/\nu$ are wall units, where y is the depth of flow, u^* the shear velocity (the shear velocity is $\sqrt{\tau_0/\rho}$, where τ_0 is the shear stress and ρ is the fluid density) and ν is the fluid viscosity]. Measurements were made using simultaneously recorded signals from the probes of two anemometers. The distances of the probes from the wall varied from $y^+ = 1.25$ to 40. Correlations were obtained with the probes up to 24η and 48η in the streamwise direction and the lateral directions, respectively, where η is the Kolmogorov microscale, $(\nu^3/\varepsilon)^{1/4}$, where the average dissipation over the entire flow, ε, was obtained from the mean flow parameters (succinctly using the rate of work on the flow per unit mass). To make the wall layer large enough to measure, highly viscous glycerine was used so that $y^+ = 5$ was 0.11 inches or about 3 mm from the wall, in a flow with a Reynolds Number based on the pipe diameter of 8700. The other components in the flow were calculated using the mixing-length assumption and the equation of continuity. The work showed that the KL expansion could elucidate the structures in the turbulent flow. The analysis concluded that the wall layer had counter-rotating eddy pairs elongated in the direction of flow and could not be considered as a totally passive, viscously dominated region. These structures combined with the turbulent flow further away from the wall. This result confirmed the hypothesis from scant correlation data [Townsend (1956)], that "attached eddies" elongated streamwise to the flow might play an important part in the control of wall turbulence.

More detailed measurements redoing the same experiment were undertaken by Herzog [1986]. This work measured four components of the correlation tensor in the wall region, though other reviews [Moin and Moser (1989)] have commented that he did not do measurements at enough points, only six points in the lateral and vertical directions and seven points in the flow direction, to have adequate convergence of the expansion. There were also several other deficiencies including the flow not being fully developed.

Following this, Chambers *et al.* [1988] carried out an analysis of flows using the data derived from Burgers' model of turbulence with Reynolds Numbers ranging from 410 to 6600, which showed that the eigenfunctions and eigenvalues of the outer layer of large-scale motions obeyed the principle of Reynolds number similarity in this range of Reynolds numbers. They also showed that the number of modes required in the expansion to give 90% of the energy increases with increasing Reynolds number for the range analyzed from four at Re = 411 to nine at Re = 6600. It also discussed the fact that the number of modes needed to be small if the KL expansion was going to reduce the size of the problem of modeling turbulence.

Moin and Moser [1989] applied the KL analysis to the results from direct numerical simulation (DNS) analysis by Kim *et al.* [1987] for a flow with a Reynolds

Number of 3100 and a depth of $y^+ = 180$. This work highlighted some differences with the laboratory measured results. It also found a weak counter-rotating pair of vortices with a narrow ejection between them. They discussed the use of the KL expansion in the DNS model instead of the Chebyshev polynomials in the vertical direction. (The spatial derivatives in the set of equations developed from the governing equations for an incompressible flow were evaluated using a spectral method.) However, they concluded that for such a model the extra computational cost would not offset the quicker convergence to give the required level of representation of energy.

Work at higher Reynolds numbers using Particle Image Velocity data was presented by Liu *et al.* [1994] and they examined the decomposition at two flows with Reynolds numbers of 5400 and 29,900. This again showed that there is a Reynolds number similarity over this range of Reynolds Number, when scaled with the outer variables in the center of the flow. The similarity did not occur in the wall layer at the boundary of the flow. The eigenfunctions were somewhat different in this part of the flow. This technique has been developed in conjunction with dynamics to produce low-dimensional models [Holmes *et al.* (1996)].

Liu *et al.* [2001] analyzed Particle Image Velocity (PIV) data that was examined by Liu *et al.* [1994], but this time in two dimensions focusing on the large-scale structures for the flow data. This work showed that about the same number of modes were required to give 50% of the energy for both Reynolds Numbers, with 13 for $\mathrm{Re} = 5378$ and 12 for $\mathrm{Re} = 29,935$, with these modes giving 67–75% of the Reynolds stress. Two-dimensional plots of the velocity correlations were also given, which showed similar patterns for both Reynolds numbers. In this analysis (and also in Liu *et al.* [1994]) there were only 60–80 photographs used. There needs to be about 400 photographs as Holmes *et al.* [1996] questioned whether 200 realizations used by Moin and Moser [1989] would be enough for statistical convergence. Therefore, 60–80 images are not enough for statistical convergence of the correlations and could (this is only conjecture) explain why less modes were required to give 50% of the energy in the lesser Reynolds number.

We develop two-dimensional covariance functions and their associated (in this case one-dimensional in the flow and vertical directions) eigenvalues and eigenfunctions necessary for the KL expansion to model the turbulence in the open channel flow. To be successful and to reduce the computation time required to simulate the turbulent field, this model would use a grid that has a larger spacing than the one required for a direct numerical simulation that was discussed by Moin and Moser [1989]. It therefore requires a model in which the KL expansion, by modeling the statistics of the turbulence, provides the closure required to set up a model of turbulence.

2. Karhunen–Loéve Expansion

The following is a brief description of the KL expansion. Other references such as Berkooz *et al.* [1993] and Bakewell and Lumley [1967] provide a more detailed

description. This section follows Chambers *et al.* [1988] and is one-dimensional to give an overview of the method. The PIV data is two-dimensional and a two-dimensional overview is given by Liu *et al.* [2001].

The KL expansion is a generalized Fourier expansion of a random field, in this case the velocity $u(x)$, using the sum of orthogonal basis functions, φ_n,

$$u(x) = \sum_{n=1}^{\infty} a_n \varphi_n(x) \tag{1}$$

with random Fourier coefficients,

$$a_n = \int_0^h u(x)\varphi_n(x)dx. \tag{2}$$

For orthogonality,

$$\int_0^h \varphi_n(x)\varphi_m(x)dx = \partial_{mn}, \tag{3}$$

where ∂_{nm} is the Kronecker delta.

Minimizing the mean square error from a partial sum of N terms (compared to the infinite number in Eq. (1)), leads to a homogeneous Fredholm equation for the basis functions,

$$\int_0^h R(x,x')\varphi_n(x')dx' = \lambda_n \varphi_n(x), \tag{4}$$

where $R(x,x') = \langle u(x)u(x')\rangle$ is the correlation function that can be derived from the PIV velocity field, and φ_n and λ_n are the eigenfunctions and eigenvalues. By Mercer's theorem,

$$R(x,x') = \sum_{n=1}^{\infty} \lambda_n \varphi_n(x)\varphi_n(x') \tag{5}$$

from which it can be shown that random Fourier coefficients are orthogonal variables with mean square values equal to the eigenvalues λ_n,

$$\langle a_m a_n\rangle = \lambda_m \partial_{nm}. \tag{6}$$

As it can be seen the procedure requires good statistical properties of the data. This means that the data must contain detailed information on the velocity field and also there needs to be many data sets. PIV is an ideal technique to obtain such data.

3. Particle Image Velocimetry (PIV) Data

The PIV data obtained for this study has a detailed velocity vector field within the water flow with data points less than 1 mm apart. The velocity field is determined by inserting neutrally buoyant silver-coated glass spheres into the flow and then taking pairs of photographs very close together, generally 75 μs for these data, with the particles being highlighted by a laser sheet pulse sent at the same time

as each photograph in the pair. At this time spacing, the particles have not moved greatly and therefore the water movement can be measured by assuming that the sphere's closest to each other from each pair of photographs is the same sphere. Cross-correlation software has been developed to undertake this analysis and also to enable bad data points to be weeded out, as these are inevitable from this technique.

Data from a laboratory undular hydraulic jump experiment by Lennon [2004] have been used to develop the model. The Reynolds number of the flow was about 24,000, with the supercritical inflow having a depth of 0.0314 m and velocity of 0.762 m/s and Froude number of 1.37. The downstream Froude number averaged about 0.75 and the depth averaged 0.047 m varying about these values along the undular waves downstream of the start of the jump.

Undular jumps do occur in nature as shown in Fig. 1 which shows a tidal bore flowing upstream on a river, in this case, as an undular hydraulic jump. The bore is moving upstream at speed in water that is flowing at a much slower rate downstream, whereas in the experimental data the water is moving and the bore is fixed in position.

The data obtained was on a square grid spaced at 0.085 mm. The data set consisted of 11 overlapping views or locations (except where there was a metal plate in the flume between two views) (see Fig. 2) of the jump each with over 5000 data points. A typical velocity field from a view is shown in Fig. 3. At each view

Fig. 1. Undular hydraulic jump River Bore on the Dordogne River (Photo: H. Chanson's web site, University of Queensland, Australia).

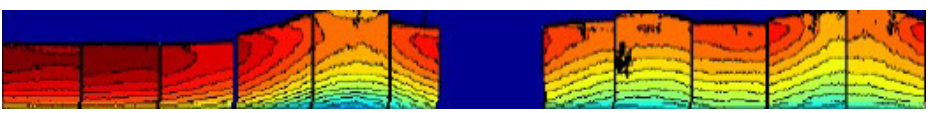

Fig. 2. Velocity field of data: (D. F. Hill, Penn State University).

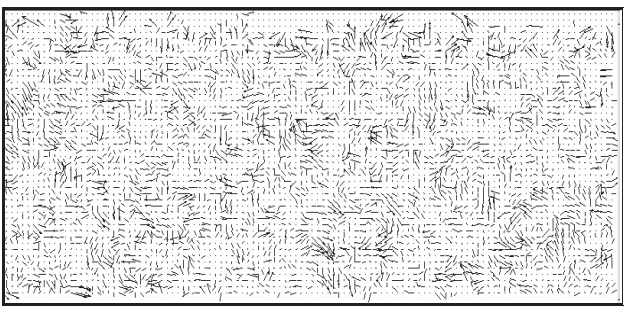

Fig. 3. Part of a velocity field obtained from a PIV analysis.

point 400 photograph pairs were taken. This enabled a good set of statistics to be obtained for each point over the whole velocity field.

Note that in Fig. 3 the mean velocities (for each horizontal line of data points) have been removed from the plot to show the flow structures and that the top 10 lines are above the water surface and appear in the data due to reflections from the water surface.

The data is in vector form, with $u(x, y)$ and $v(x, y)$, where u and v are the x and y velocities, respectively, and x and y are the x and y positions on the domain. The time step between each pair of photographs was about 1 s which meant that the data between time steps cannot show the development of the flow structures as the flow has changed too much between each photograph. This was not an issue to develop the covariance functions from the flow statistics of the data sets. The data in terms of wall units is spaced on a grid that is equal to about $y^+ = 31.5$ units. This means that the lowest values are just on the upper side of the buffer layer well above the viscous wall region ($y^+ < 5$).

The flow fluctuations have been analyzed over the period when they were taken and this shows that the flow is constant over the time period. If a 10-point moving average of the velocity using the 400 image pairs are plotted (as shown in Fig. 4), they do not show any significant change over the length of the series and do not plot outside three standard deviations above or below the mean.

However, if the mean velocity profiles for locations 1, 2, and 3, as shown in Fig. 5 are examined, this shows discontinuities in velocities between each location, i.e. the velocities at the downstream end of Location 1 and the upstream end of Location 2 do not match.

This means that the flow and hence velocities were fluctuating over time. This was probably not visibly apparent in the experiments when the measurements were taken, however fluctuations became apparent when a wave gauge was inserted into the flow to measure water levels. This should not be the case as described in Tursunov [1969] in which he states that the waves should be static.

If the flow is fluctuating, the continuity between Location 1 and Location 2 should be satisfied. Examination of the depth profile in Fig. 4.2 of Lennon [2004]

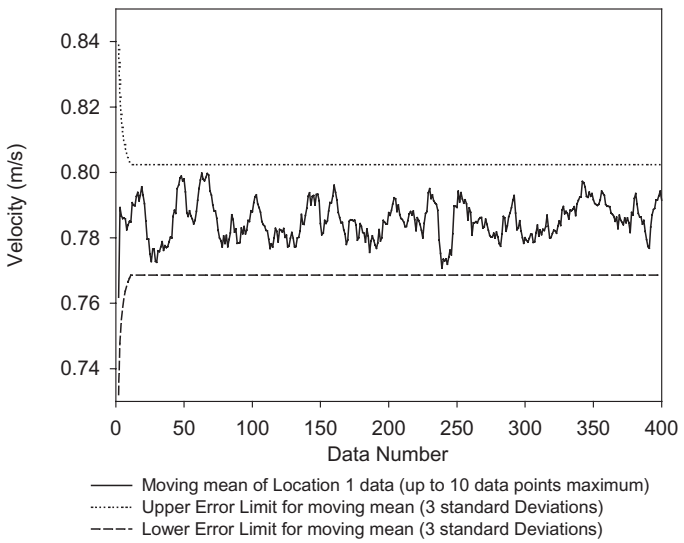

Fig. 4. Moving average control chart for 10 values of velocity for the 400 image pairs taken at Location 1.

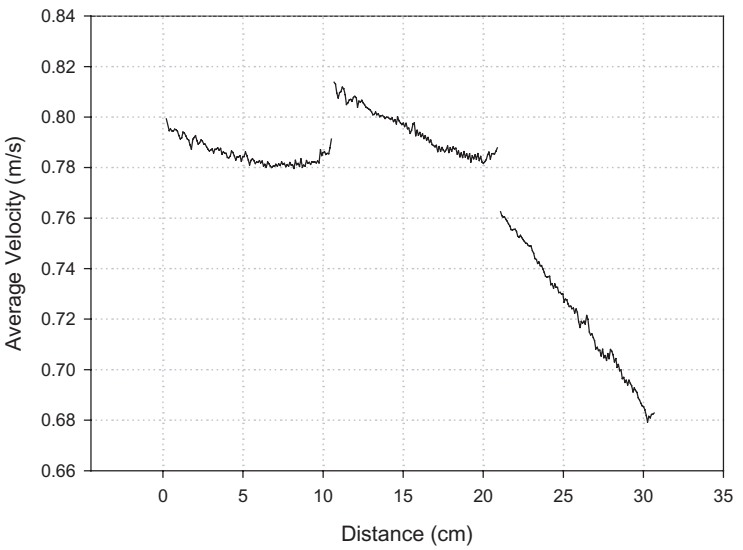

Fig. 5. Average velocities of each verticals in Locations 1 (0–10 cm), 2 (11–21 cm), and 3 (21–31 cm).

shows a drop in depth between the downstream end of Location 1 and the upstream end of Location 2. Using these measured values of depth, a plot of the volume continuity was built, as shown in Fig. 6. This indicates that the flow or discharge per unit width is almost the same between Location 1 (0.2–10.5 cm) and Location 2 (10.7–20.9 cm), and also part of Location 3 (20.1–30.7 cm).

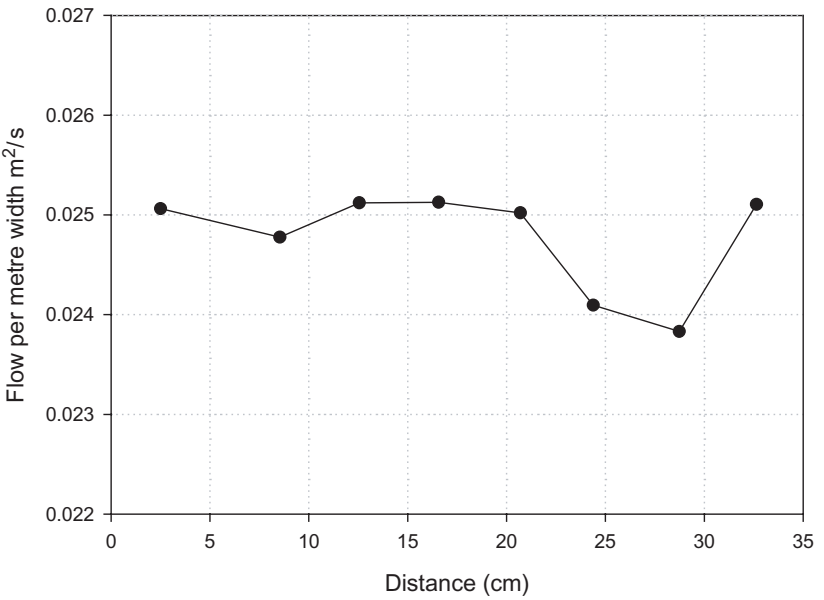

Fig. 6. Flow continuity calculations from x-velocity and depth measurements.

It is also noted here that Fig. 5 shows a slowing of velocity along the streamwise direction. This was due to the flow approaching the jump. This means that the flow, although close to steady or stationary, was not uniform in this area.

3.1. *Turbulence intensities of data or variance of data*

This nonuniformity of the flow may be the probable reason for the universal law of turbulence intensity [Nakagawa *et al.* (1975); Nezu and Nakagawa (1993)] not obeyed in these two locations (1 and 2) that are in the supercritical flow region of the jump. A plot of the turbulence intensities of Locations 1, 2, and 3 and the universal law of turbulence intensity versus the depth are shown in Fig. 7. This result for Location 1 was presented by Lennon [2004], though no reason was given. Note that the formula for the universal turbulence intensity, $\frac{u'}{u^*} = D_u \exp\left(-\lambda_u \frac{y}{h}\right)$ is based on the average value of this ratio over the log-law region of the flow up to $y = 0.3$ depth, where u^* = shear or friction velocity, $D_u = 2.3$ and $\lambda_u = 1.0$ for the flow in the streamwise direction (there are different values for these coefficients in the vertical and lateral directions). The value of friction velocity was calculated from the bulk velocity and Dean's coefficient that was calculated from the Reynolds number.

This is a very important point, as the intensities in both Locations, 1 and 2 (and also Location 3), are well away from the standard profiles that are based on the log-law as shown in Fig. 7. The value of u' is very closely related to the KL analysis as

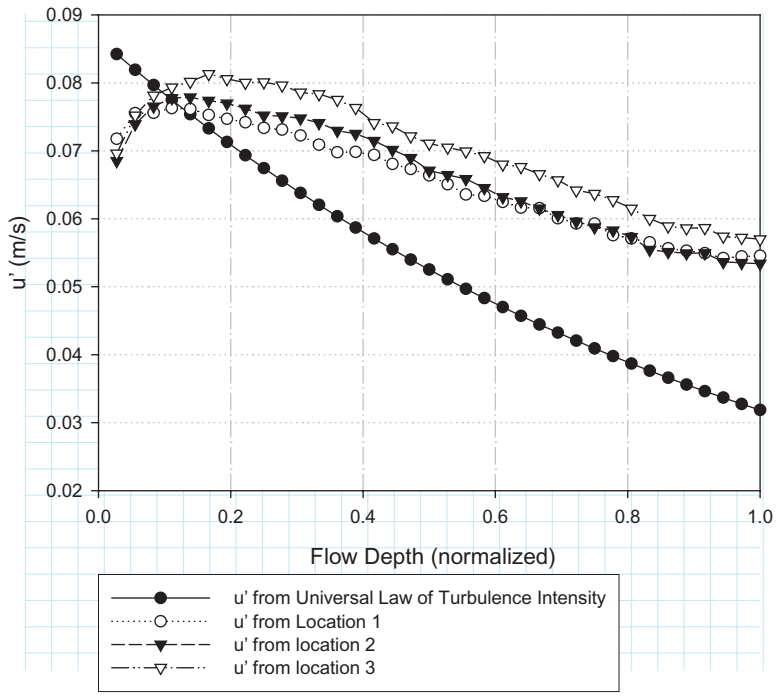

Fig. 7. Plot of u' versus depth for Locations 1, 2, and 3 compared with the expected u' from the Universal Law of Turbulence intensity.

u'^2 is the variance σ^2, of Eq. (21) in Sec. 4.3. This means that any model developed from this data will not have the standard velocity profile for uniform flow.

The difference in turbulence intensity profiles is an interesting phenomenon as it shows that the subcritical influence of the undular waves is influencing the upper parts of the flow profile in the supercritical flow area. This was the only jump in the work of Lennon [2004] that had this phenomenon, as the laboratory data collected for two other hydraulic jumps showed the upstream supercritical flow turbulence intensities that matched the universal turbulence intensity law very well.

4. Analysis

4.1. *Two-point correlation functions — Covariance structure*

Analysis of the covariance structure of the velocity field was undertaken by developing a software within the Matlab program [MathsWorks (2006)].

In each field two-dimensional two-point velocity correlations were calculated in both the flow direction and the vertical direction. This was undertaken for five depths (in some cases more) in the flow arbitrarily chosen to enable a covariance or correlation function to be derived that covered the complete depth of flow. The data at each depth was averaged over an ensemble of 200 of the data sets

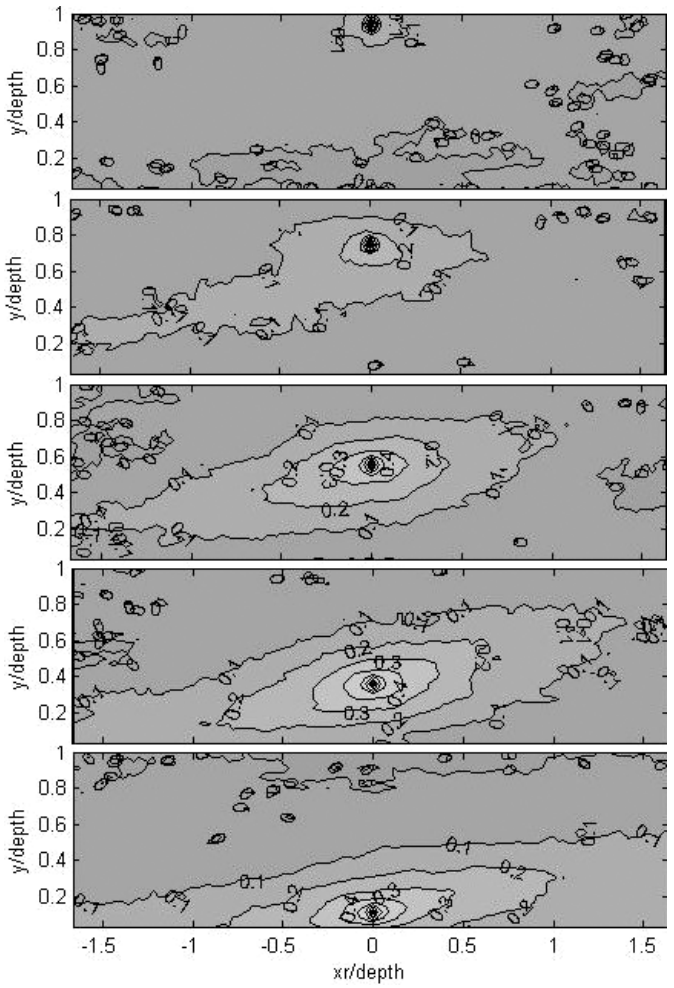

Fig. 8. x-velocity correlation plots at five depths in the flow ($y = 0.11$ h, 0.36 h, 0.55 h, 0.75 h and 0.94 h) for Location 1 (h stands for depth).

for each field. There were points where data were missing and these were eliminated from the calculations. The results are shown for Location 1 or velocity field in Fig. 8.

As can be seen from Fig. 8, the x-velocities of the flow are strongly correlated over a considerable distance upstream and downstream at an angle of about 8° with the bed. This angle is probably due to the flow structures arising from the bed. These structures are known as sweeps and bursts and they have a strong effect on the average velocity in the field as it varied between data sets of a complete view from 0.7 m/s to 0.84 m/s (a 20% range) for a length of flow that was three times the depth.

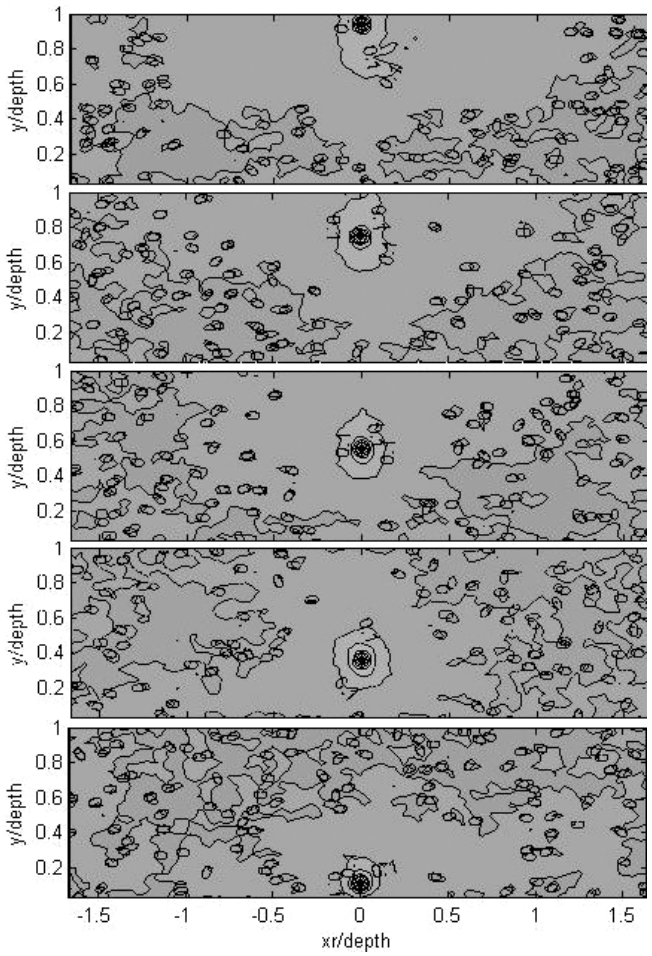

Fig. 9. y-velocity correlation plots at five depths in the flow ($y = 0.11$ h, 0.36 h, 0.55 h, 0.75 h, and 0.94 h) for Location 1.

However, the plots in Fig. 8 also show that in the top 10% of the flow, the x-velocity correlation distance is small and is similar to the y-velocity correlation distances shown in Fig. 9.

The correlation distances shown in Fig. 9 are not great and this reflects the size of the correlations in the vertical direction. The average y-velocity did not change significantly from data set to data set, whereas the x-velocity did vary by up to 20% between data sets. This meant that when the ensemble averaging took place the x-velocity correlation distances were much larger than if just sample averaging was used.

These correlation plots are very similar to those calculated by Liu *et al.* [2001] for the flow between two plates with a similar Reynolds number.

4.2. *Covariance function*

An analytical covariance function (kernel) was developed that gave a good fit to the covariance kernels obtained from the data.

4.2.1. *Function form*

Two types of functions were considered. Both these had an elliptical shape to them. The first form of the function was

$$Z = e^{-\lambda r^k}, \tag{7}$$

where Z is the value of the correlation function, λ is a factor to allow for the drop-off in correlation with distance "r" which equals $|x_1 - x_2|$ in a one-dimensional case or $\sqrt{x_c^2 + y_c^2}$ in the two-dimensional case, where x_c and y_c are defined as shown in Fig. 11. The exponent of "r" is "k".

However, it was not possible to solve the homogeneous Fredholm equation analytically with this equation as the kernel had a value of 0.5 for "k". In addition, the above equation had poor fit to the data in the top-half of the flow, for example, the percentage of the variance explained at 0.75 depth was only 38.5%.

Therefore, another form of equation was adopted as given in Eq. (8) below:

$$Z = ae^{-\lambda_1 r} + (1 - a)e^{-\lambda_2 r}. \tag{8}$$

This formula gave a better fit over the complete profile with a minimum of 81% of the variance explained at 0.75 of the depth as shown in Table 1.

It is noted here that the covariance of turbulence at the origin (where $x = 0$) should be smooth [Pope (2000)], whereas this function is not smooth at the origin.

Table 1. Best fit values for the parameters $\lambda_{x1}, \lambda_{x2}, f_{r1}, f_{r2}$ and "c" using Genstat.

$Y1 = y/\text{depth}$	a_1	λ_1	λ_2	c	f_1	f_2	% variance
0.02778	0.3962	−0.5129	−24.55	−0.0925	7.126	1.07	95.7
0.055556	0.4111	−0.65	−20.3	−0.124	6.68	1.16	96.9
0.11111	0.436	−0.799	−19.7	−0.1336	5.916	1.176	97.7
0.25	0.4458	−0.9571	−20.98	−0.152	4.697	1.07	96.4
0.36111	0.447	−1.154	−26.78	−0.171	4.186	0.803	94.2
0.41667	0.4333	−1.2146	−28.84	−0.158	3.988	0.8255	92.7
0.47222	0.4254	−1.32	−34.29	−0.1829	3.663	0.793	91.2
0.56666	0.3715	−1.364	−36.56	−0.2033	3.453	0.815	89.1
0.58333	0.3462	−1.399	−34.57	−0.2126	3.224	0.8679	87.1
0.63889	0.2747	−1.248	−31.56	−0.2199	3.222	0.933	85.7
0.69444	0.2232	−1.073	−29.54	−0.2583	3.15	1.03	82.2
0.75	0.184	−1.036	−31.49	−0.321	2.631	1.018	81
0.77778	0.186	−1.089	−35.11	−0.3337	2.639	0.971	84.3
0.83333	0.1456	−0.9486	−36.12	−0.333	2.553	0.9577	84.2
0.88889	0.1349	−1.327	−39.6	0.0063	2.068	0.937	88.6
0.94444	0.1108	−1.086	−40.67	−0.0046	2.797	0.886	85.7
1.000	0.096	−0.9517	−39.0	0.1695	2.890	0.9207	82.3

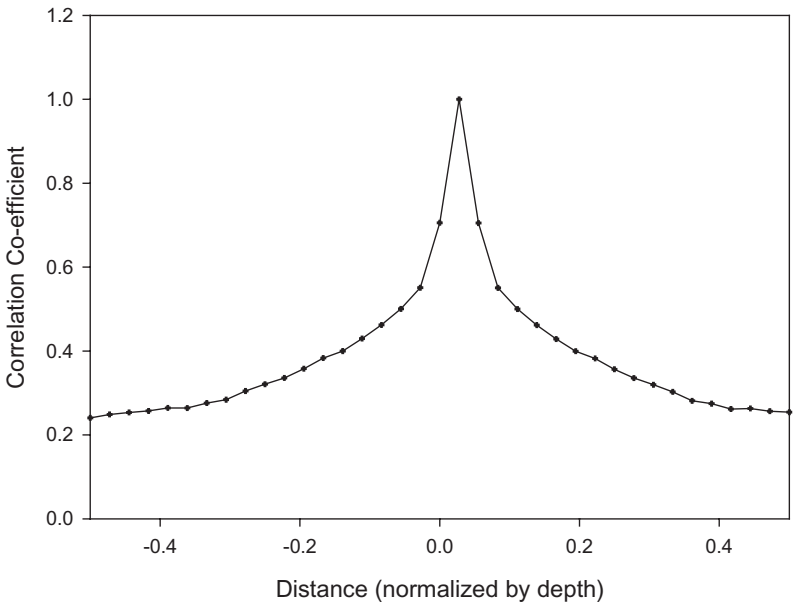

Fig. 10. Covariance (Correlation coefficient) verses distance for Location 1 data at 0.1111 depth.

However, the data does not show this smoothness as the points are too far apart. The covariance of the adjacent points was considerably below unity as shown in Fig. 10.

4.2.2. *Ellipse equation*

It is noted that the function is in the form of an ellipse. Ellipses have an equation of general form of

$$\frac{x^2}{a^2} + \frac{y^2}{b^2} = 1, \tag{9}$$

where a is the distance along the x-axis and b is the distance along the y-axis of the ellipse.

As shown in Fig. 11, "$p1$" is the point where the correlations are taken from and "$p2$" is an arbitrary point on the ellipse. The distance between these points is "r". It has two components "xc" and "yc" that are easily calculated from the data.

If a value of Z is the same at "m" and "n" on the x- and y-axes respectively, then

$$Z_m = e^{\lambda_x r_x} = e^{\lambda_y r_y} = Z_n. \tag{10}$$

Noting that λ_x is negative,

$$r_x = \frac{a}{b} r_y \quad \text{or} \quad r_x = f r_y, \text{ where } f = \frac{a}{b}. \tag{11}$$

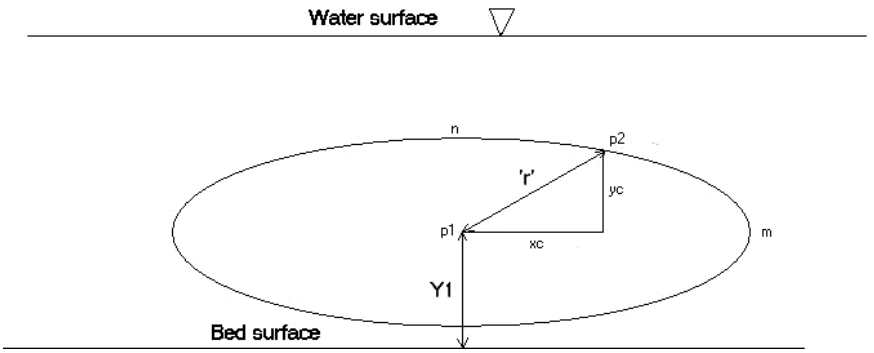

Fig. 11. Various definitions for data fitting to an ellipse.

Then it is easily shown that,

$$\lambda_x f = \lambda_y, \tag{12}$$

i.e. the change in λ is proportional to the distance "r" from point "$p1$".

The next step was to find out how λ varies when point "$p2$" changes position. The first step in this analysis was to find a relationship between x-axis and y-axis values of λ. This can be done by replacing either "a" and "b" with "r", in this case replacing "b" with "r" to give

$$\lambda_x \frac{a}{r} = \lambda_{p2}. \tag{13}$$

As $f = \frac{a}{b}$, the ellipse formula (using xc and yc) becomes

$$\frac{xc^2}{f^2 b^2} + \frac{yc^2}{b^2} = 1, \tag{14}$$

giving

$$a = f\sqrt{\frac{xc^2}{f^2} + yc^2}. \tag{15}$$

But we can use "a" as "xc" and "yc" are given values

$$Z = e^{\lambda_{p2} r} = e^{\lambda_x \frac{a}{r} r} = e^{\lambda_x a}, \tag{16}$$

where "a" is defined by Eq. (15).

4.2.3. *Fitting the ellipse at an angle "c"*

The definitions to change the angle of the ellipse are given in Fig. 12.

The ellipse can be fitted at an angle by using a transformation formula for rotation,

$$x_r = xc(\cos(c)) + yc(\sin(c)) \tag{17}$$

$$y_r = yc(\cos(c)) - xc(\sin(c)). \tag{18}$$

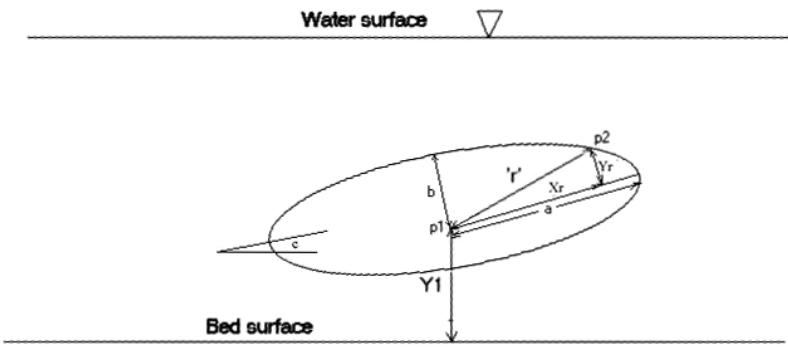

Fig. 12. Definitions for fitting to an ellipse at angle "c".

The xc and yc of Eq. (15) can be replaced by x_r and y_r of Eqs. (17) and (18) to obtain a value for "a" and the resultant placed in Eq. (16) and that into Eq. (8) form giving

$$Z = a_1\, e^{\lambda_{x1}\left(f_{r1}\sqrt{\frac{x_{r1}^2}{f_{r1}^2}+y_{r1}^2}\right)} + (1-a_1)e^{\lambda_{x2}\left(f_{r2}\sqrt{\frac{x_{r2}^2}{f_{r2}^2}+y_{r2}^2}\right)}, \tag{19}$$

where "f_r" is the ratio of "a" and "b" along the rotated ellipse shown in Fig. 12. In this formula "c" is calculated from y_{r1} and y_{r2}, and f_{r1} and f_{r2}.

4.2.4. *Fitting whole range of depths*

The best values of λ_{x1}, λ_{x2}, f_{r1}, f_{r2}, and "c" can be determined by analysis using a nonlinear fitting analysis computer program, in this case "Genstat" [VSN (2006)].

Finally this analysis can be done for each level and the changes in these parameters over the normalized depth "$Y1$" calculated. The results are shown in Table 1 and the curves derived from these results are shown in Figs. 13–18.

An equation for the whole field using the equation orders of the "best fit for initial equations" (using Microsoft Excel) as shown in Figs. 13–18, as templates, was calculated using a nonlinear fitting technique in the program, Genstat [VSN (2006)]. The final form is shown in Eq. (20) and is also shown in Figs. 13–18 labeled as the "Genstat fit". Note that "c" was chosen to be a constant. Also the value of "f_2" for the Genstat fit is above the best initial fit. This was due to this factor having little weight. The results do not change significantly with a value of 1.0 for f_2 that assumes this kernel is round which is the case for isotropic turbulence.

$$\begin{aligned} Z = {} & (a_{12}Y_1^2 + a_{10})e^{(\lambda_{10}+\lambda_{11}Y1+\lambda_{12}Y_1^2)\left((f_{r10}+f_{r11}Y1)\sqrt{\frac{x_r^2}{(f_{r10}+f_{r11}Y1)^2}+y_r^2}\right)} \\ & + (1 - a_{12}Y_1^2 + a_{10})e^{(\lambda_{20}+\lambda_{21}Y1)\left((f_{r2})\sqrt{\frac{x_r^2}{(f_{r2})^2}+y_r^2}\right)}. \end{aligned} \tag{20}$$

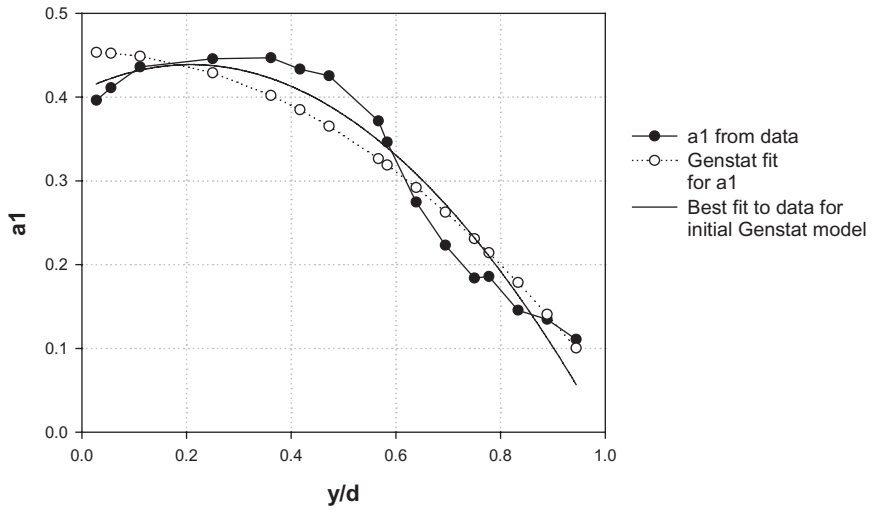

Fig. 13. Location 1 — Fit for a_1 with depth.

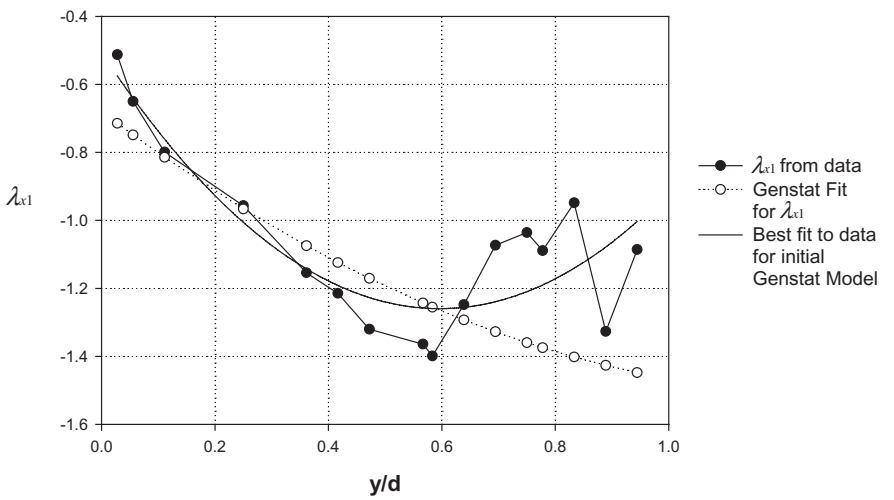

Fig. 14. Location 1 — Fit for λ_{x1} with depth.

The analysis gives an R^2 value of 0.906 for Location 1 and 0.896 for Location 2 with slightly different values of the parameters. These are shown in Table 2.

Note that in the Genstat analysis some of the parameters were limited to close to best fit equations; otherwise the program would not converge. This was not seen as a problem as the percentage of the variance explained with the derived function was 90.6% for Location 1 and 89.6% for Location 2. A plot of the kernel covariance

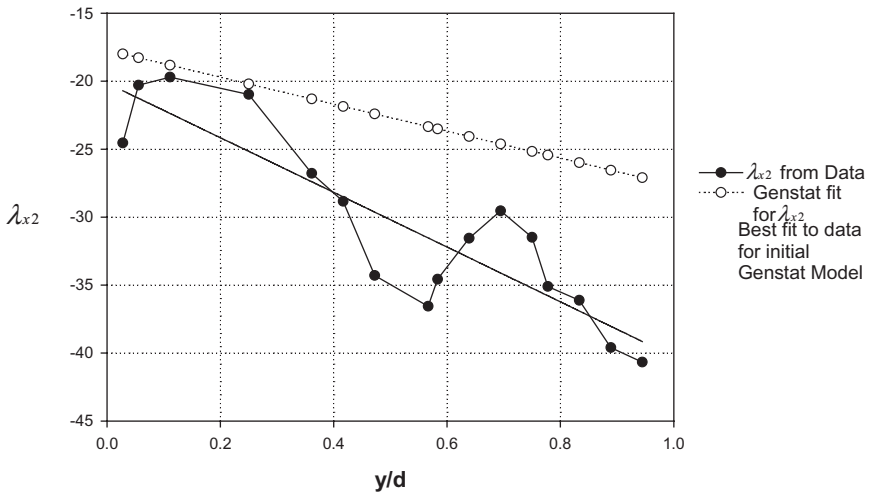

Fig. 15. Location 1 — Fit for λ_{x2} with depth.

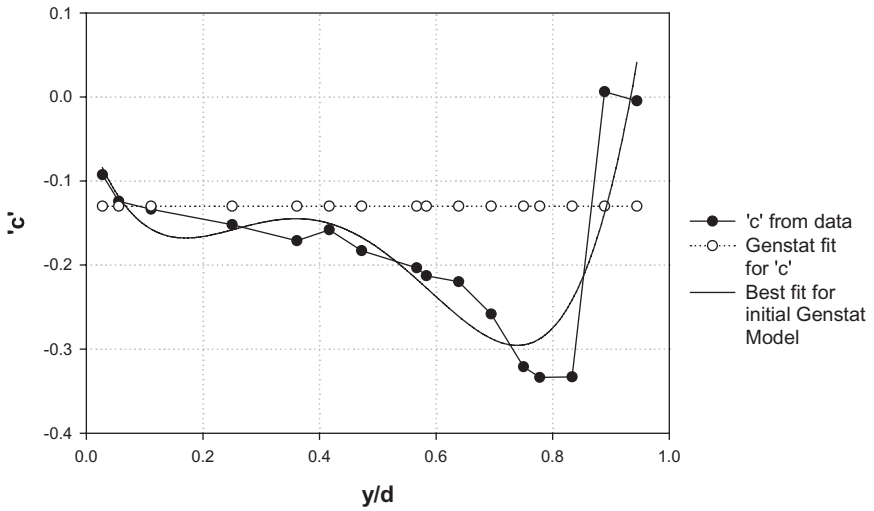

Fig. 16. Location 1 — Change in "c" with depth.

function for kernel of the x-direction velocity correlation function Location 1 is shown in Fig. 19. This can be compared to Fig. 8.

A plot of the kernel covariance function for kernel of the x-direction velocity correlation function Location 1 is shown in Fig. 20. This can be compared to Fig. 9.

This kernel in the y-direction has been calculated using Eq. (20). This has only given a reasonable fit with just under 70% of the variance explained.

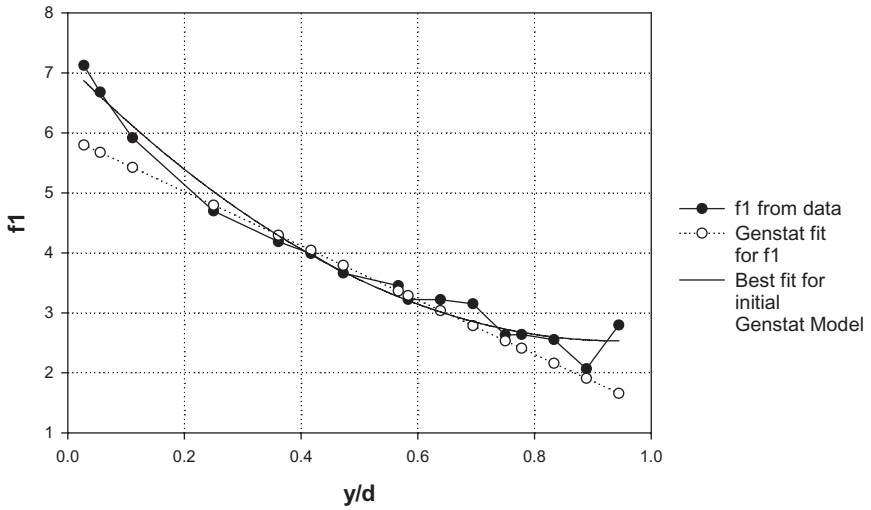

Fig. 17. Location 1 — Change in ellipse ratio, "f_1" with depth.

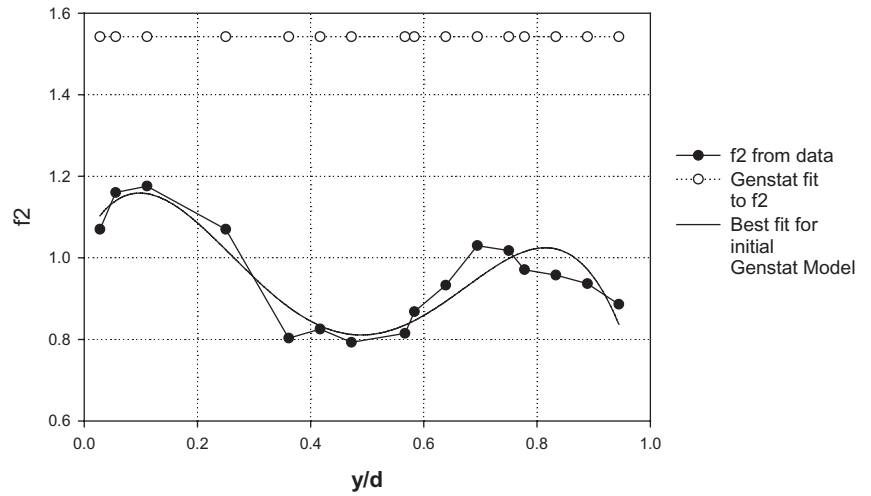

Fig. 18. Location 1 — Change in ellipse ratio, "f_2" with depth.

4.3. *Eigenfunctions*

The eigenvalues and eigenfunctions were solved analytically in this paper using the covariance kernel obtained earlier. This made it easier to understand the processes taking place in the flow and how the random process changes over the turbulent velocity field.

The main problem faced was solving a kernel that is the addition of two exponential functions. If the kernel consists of one exponential function then the solution

Table 2. Values of parameters for best fit for kernel of the velocity correlations for Locations 1 and 2 data.

Factor	Value for Location 1	Value for Location 2
a_{12}	−0.39204	−0.37002
a_{10}	0.45033	0.42833
l_{12}	0.8813	1.2228
λ_{11}	−1.5354	−1.7287
λ_{10}	−0.65173	−0.43336
λ_{21}	−8.747	−9.434
λ_{20}	−18.417	−16.592
f_{r11}	−4.3181	−5.7717
f_{r10}	5.8832	6.6159
f_{r2}	1.5418	1.6246

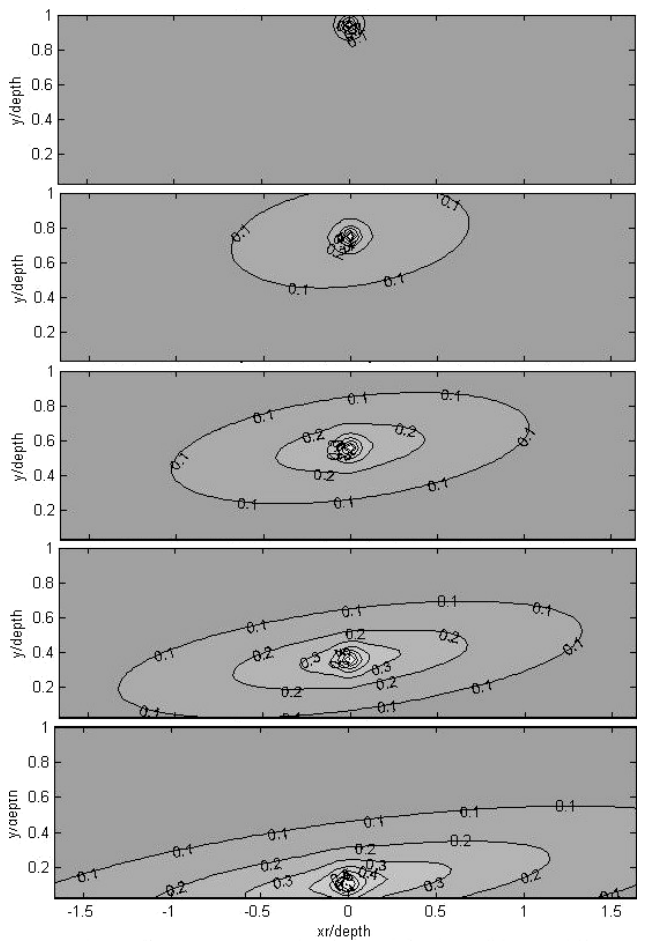

Fig. 19. Plot of x-velocity covariance kernel (normalized to the correlation coefficients) as calculated by Eq. (20) ($y = 0.11$ h, 0.36 h, 0.55 h, 0.75 h and 0.94 h) for Location 1.

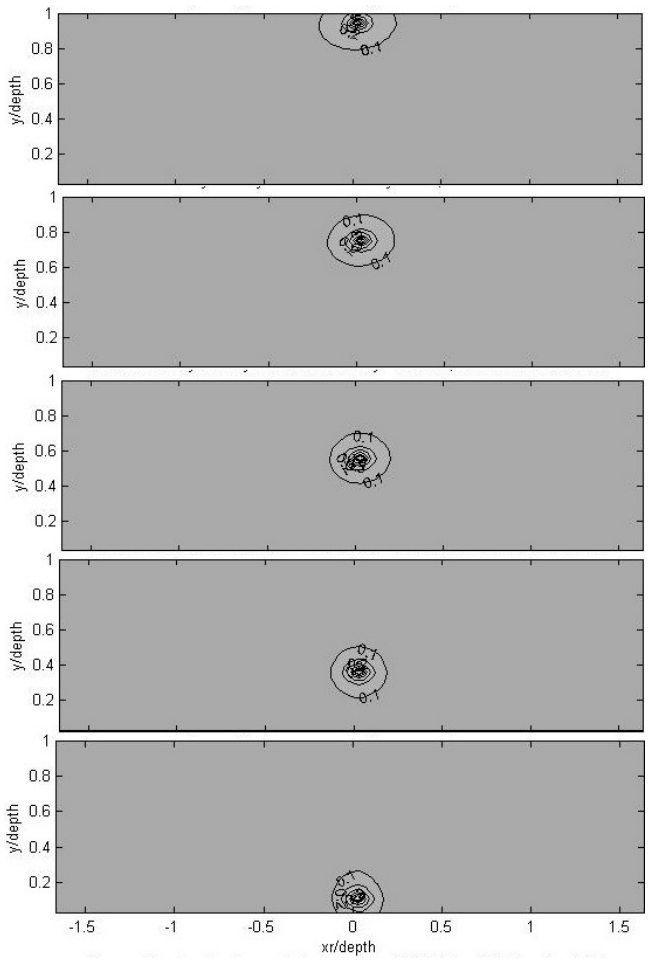

Fig. 20. Plot of y-velocity covariance (normalized to the correlation coefficients) kernel as calculated by Eq. (20) ($y = 0.11$ h, 0.36 h, 0.55 h, 0.75 h, and 0.94 h) for Location 1.

is as given by Kulasiri and Verwoerd [2002]. Each part of the kernel can be solved using this method with the Fredholm equation in the form outlined in Eq. (4) giving

$$\int_0^a \sigma^2 e^{-\lambda_1|x_1-x_2|}\phi_1(x_2) = \mu_1\phi_1(x_1) \tag{21}$$

for the first part of the kernel, where σ^2 is the variance, and

$$\int_0^a \sigma^2 e^{-\lambda_2|x_1-x_2|}\phi_2(x_2) = \mu_2\phi_2(x_1) \tag{22}$$

for the second part of the kernel.

This means that μ_1 and $\phi_1(x_1)$, and μ_2 and $\phi_2(x_1)$ can be calculated.

Now a function needs to be found that gives the same result as the sum of the pair of eigenfunctions and eigenvalues, i.e.

$$\int_0^a \sigma^2 e^{-\lambda_1|x_1-x_2|} f_1(x_2) + \int_0^a \sigma^2 e^{-\lambda_2|x_1-x_2|} f_1(x_2) = \mu f_1(x_1). \tag{23}$$

Therefore, approximately,

$$\mu_1\phi_1(x_1) + \mu_2\phi_2(x_1) = \mu f(x_1). \tag{24}$$

However, for orthonormality the following is true:

$$\int_0^a f(x_1)^2 = 1. \tag{25}$$

Hence, from Eq. (24),

$$\int_0^a \left\{ \frac{\mu_1\phi_1(x_1) + \mu_2\phi_2(x_1)}{\mu} \right\}^2 dx_1 = 1, \tag{26}$$

giving,

$$\mu^2 = \int_0^a \{\mu_1\phi_1(x_1) + \mu_2\phi_2(x_1)\}^2 dx_1. \tag{27}$$

And as orthonormality also means,

$$\int_0^a \phi_1(x_1)^2 dx_1 = 1, \tag{28}$$

$$\int_0^a \phi_2(x_1)^2 dx_1 = 1. \tag{29}$$

Evaluating the squared term gives

$$\mu^2 = \mu_1^2 + \mu_2^2 + \mu_1\mu_2 \int_0^a \phi_1(x_1)\phi_2(x_1) dx_1. \tag{30}$$

The integral evaluation and details are given in Appendix A.

Using the solution in Appendix A, the eigenfunctions are in the form

$$\frac{1}{\mu}\left(\frac{\mu_1}{\sqrt{N_1}} \left[\sin(w_1x_1) + \frac{w_1}{\lambda_1}\cos(w_1x_1) \right] + \frac{\mu_2}{\sqrt{N_2}} \left[\sin(w_2x_1) + \frac{w_2}{\lambda_2}\cos(w_2x_1) \right] \right). \tag{31}$$

These are plotted in Fig. 21.

These are very similar to the eigenfunctions calculated numerically by Liu *et al.* [1994] except for the first function. The functions given by Liu *et al.* [1994] are zero at zero on the distance axis which in their case is the bed of the flow as the functions are derived for the nonhomogeneous vertical direction.

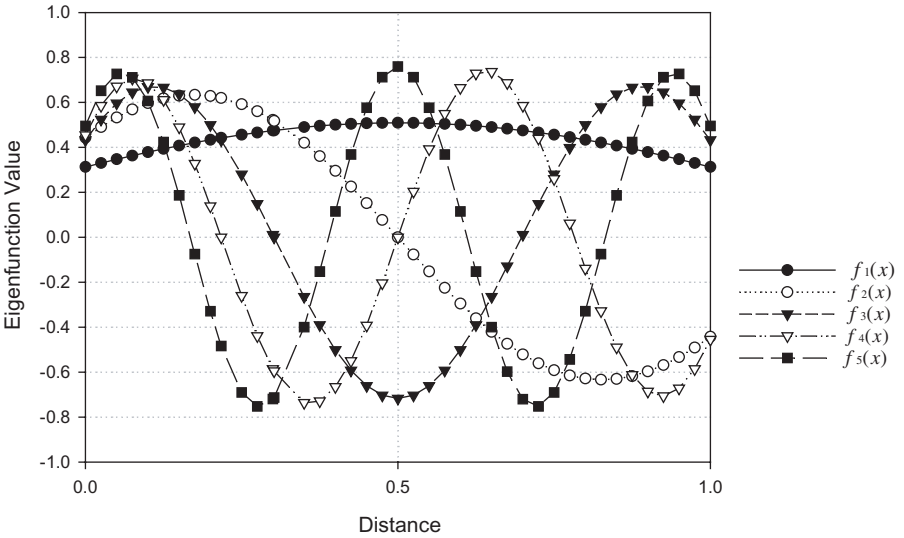

Fig. 21. The first five eigenfunctions.

5. Double Kernel Structure

In this section, the relationship between the double kernel structure and the turbulence production and dissipation are investigated.

If kernel equation, Eq. (20) is examined, it has two terms. The first term (with the smaller negative λ value) relates to the points that are more distant than the second term. Therefore we will call the first term the "outer part" of the kernel and the second part the "inner part" of the kernel. If Fig. 13 is examined this shows that the influence of the "outer kernel" drops off over the upper half of the flow. This means that the "inner kernel" now becomes predominant. This is despite the "inner kernel" coefficient a_1, having the largest coefficient over the whole flow as the value of a_1, the coefficient for the outer part of the kernel only reaches a maximum of 0.45. This means that the value of the coefficient for the inner part of the kernel is 0.55 or greater. This can be thought of as the ratio of the outer and inner kernels. The ratios of inner and outer kernels are plotted for the complete range of values over the flow depth in Fig. 22.

The outer part of the kernel results from the larger structures in the flow and the inner part of the kernel from the smaller structures in the flow. Hence, the outer kernel could be primarily related to the turbulent production structure range or the largest structures in the flow, while the inner kernel could be primarily related to the turbulent dissipation range.

This is found to be the case as Fig. 22 also has two curves from Fig. 3 of Moser *et al.* [1999] showing the ratio of turbulence production to turbulence dissipation for two similar flows which in this case have smaller values of Re_τ of 590 and 395

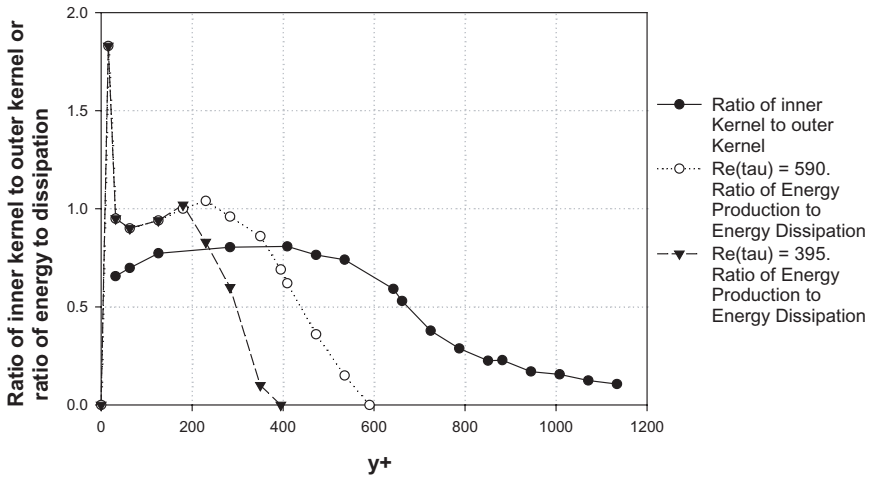

Fig. 22. Ratio of inner and outer kernels of Location 1 and ratio of turbulence production vs turbulence dissipation for $Re_\tau = 590$ and 395 [Moser *et al.*, 1999].

compared to 1188 for this data. The two curves show a shape similar to the ratio of kernels over the flow profile. The ratio of inner and outer kernels has a broader plateau in the log-law region, due to the larger Re_τ value and drops off above this region as the data given by Moser *et al.* [1999] also does.

The ratios are a little different as expected, as both parts of kernel contain covariances relating to flow structures in the inertial range. This is investigated in more detail to compare the dissipation and production ranges with the two parts of the kernel.

To calculate the dissipation range the following analysis was undertaken. Firstly the rate of dissipation was calculated using the rate of work per unit mass (per unit channel width neglecting the channel sides) as outlined by Bakewell and Lumley [1967]. This gives $\eta = 0.075$ mm or about three viscous or wall units. From the calculations of u' from the data, varying from 55 mm near the surface, to 75 mm near the bed, Taylor Scales were calculated of 1.2 mm and 1.6 mm, respectively. This gives the Taylor Scale Reynolds Number varying from 65 near the surface to 122 near the bed. From Fig. 6.21 of Pope [2000] this gives the turbulence dissipation range being the scales below about 40η or about 3 mm that is about 10% of the flow depth.

(Note that this gives the ratio of Taylor scale Reynolds number varying from $Re = 1.6R_\lambda^2$ at the bed to $5.5R_\lambda^2$ at the surface. This is compared reasonably with $Re = 1.2R_\lambda^2$ at the bed to $9R_\lambda^2$ at the surface calculated using $Re_T = \frac{u' L_{11}}{\nu}$, where L_{11} is the longitudinal integral length scale that is calculated by integrating the correlation functions at the bed and the surface ($y = 0.027778$ d and 1.0 d) obtained from the data and shown in Table 1 and the relationship between Re_T and Re_L [Pope (2000)].)

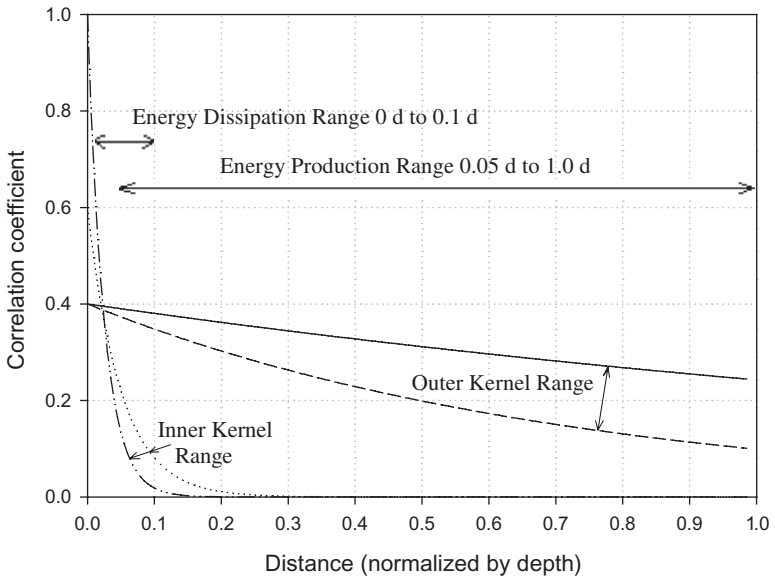

Fig. 23. Inner and outer kernel correlations and ranges normalized by depth.

The turbulent production range is for structures above about $\frac{1}{6}\ell_0$ [Pope (2000), p. 184], where ℓ_0 is comparable with the flow depth or the structures, however ℓ_0 is not defined. However, this can be approximately assessed using figure 6.21 in the study by Pope [2000] as this shows that the energy production range overlaps considerably with the dissipation range and includes structures larger than about 20η or about 5% of the flow depth. This means there is an overlap region between 20η and 40η, (5% and 10% of the flow depth) where both production and dissipation occur.

When this is compared to the covariance structure it can be seen that a sizable portion of the inner part of the kernel contains energy production structures which are greater than 5% of the flow depth as shown in Fig. 23.

The outer kernel contains some dissipation structures but not to the same extent as the inner kernel contains energy producing structures. Therefore, the inner kernel contains almost all the dissipation structures and some of the energy production structures, and it will have a larger weighting than the outer kernel that contains most of the energy production structures. This is put forward as a tentative explanation for the reason that the maximum ratio of the outer to inner kernel is less than the maximum ratio of turbulence production to dissipation.

6. Conclusions

An analysis was performed on the PIV data collected on the approximately uniform flow just upstream of an Undular Hydraulic Jump. It checked the properties of the

data and also determined the covariance to enable a KL expansion to be undertaken for a turbulence model.

Analysis of the data set showed that it was stationary in time for the period when the PIV data was collected at each position, but it was not stationary between changing camera locations even though the discharge did not change. This means that there was a very slow change in flow properties during the experiments. The flow was also neither uniform nor did it have any standard values of turbulent fluctuations in the locations analyzed as they were close to the Undular hydraulic jump.

The analytical analysis of the covariances of the ensemble of 200 of the 400 data sets found that the covariances had elliptical shapes. The best covariance kernel that was found had two parts to it, and gave a much better fit over the flow compared to a kernel that only had one part. The equation fitted to the kernel, for the complete two-dimensional data, was developed based on the ellipse and this gave a good fit with an R^2 value around 0.9 for the data. This kernel gives the covariance at any point in the flow.

An approximate solution to this equation was developed but only in the one-dimensional sense. The eigenfunctions and eigenvalues were evaluated for the two-part kernel using the orthonormality properties of both parts on the kernel and the complete kernel. Future work will analyze the vector data numerically using techniques available to find a two-dimensional eigenfunctions and eigenvalues to develop random fields and also to develop a model from these.

The two parts of the kernel were found to strongly correlate with the ratio of turbulence production and turbulence dissipation with a likely explanation of the differences being due to the overlapping range of scales that have both production and dissipation and the scales relating the two kernel parts.

Acknowledgments

Acknowledgment is given to the New Zealand Tertiary Education Commission for assistance with funding for the first author's PhD scholarship.

The authors would like to thank the staff and students at the C-fACS center for advice and discussions about the work, especially Wynand Verwoerd. Lastly the author would like to thank the innumerable people who kindly put information on the internet that solved many issues and problems associated with this work.

Appendix A

The integral in Eq. (30) becomes

$$\frac{1}{\sqrt{N_1 N_2}} \int_0^a \left[\sin(w_1 x_1) + \frac{w_1}{\lambda_1}\cos(w_1 x_1)\right] \left[\sin(w_2 x_1) + \frac{w_2}{\lambda_2}\cos(w_2 x_1)\right]. \quad \text{(A.1)}$$

Evaluating the integral gives

$$\frac{1}{\sqrt{N_1 N_2}}\left[\begin{array}{l}\left(\dfrac{1}{w_2^2-w_1^2}\right)\left[w_1\cos(w_1a)\sin(w_2a)-w_2\sin(w_1a)\cos(w_2a)\right]\\ +\dfrac{w_1}{\lambda_1}\left(\dfrac{1}{w_1^2-w_2^2}\right)\left[w_1\sin(w_1a)\sin(w_2a)+w_2\cos(w_1a)\cos(w_2a)\right]\\ +\dfrac{w_2}{\lambda_2}\left(\dfrac{1}{w_2^2-w_1^2}\right)\left[w_2\sin(w_1a)\sin(w_2a)+w_1\cos(w_1a)\cos(w_2a)\right]\\ +\dfrac{w_1w_2}{\lambda_1\lambda_2}\left(\dfrac{1}{w_2^2-w_1^2}\right)\left[w_2\cos(w_1a)\sin(w_2a)-w_1\sin(w_1a)\cos(w_2a)\right]\\ -\left[\dfrac{w_1w_2}{\lambda_1}\left(\dfrac{1}{w_1^2-w_2^2}\right)+\dfrac{w_1w_2}{\lambda_2}\left(\dfrac{1}{w_2^2-w_1^2}\right)\right]\end{array}\right]. \tag{A.2}$$

References

Bakewell, P. and Lumley, J. L. [1967] Viscous sublayer and adjacent wall region in turbulent pipe flows, *Phys. Fluids* **10**, 1880–1897.

Berkooz, G., Holmes, P. and Lumley, J. L. [1993] Proper orthogonal decomposition in the analysis of turbulent flows, *Annual Review of Fluid Mechanics*, ed., Sears, W. R. (Annual Reviews Inc, Palo Atlo, Calif), Vol. 25, pp. 539–575.

Chambers, D. H., Adrian, R. J., Moin, P., Stewart, D. S. and Sung, H. J. [1988] Karhunen–Loeve expansion of Burger's model of turbulence, *Phys. Fluids* **31**(9), 2573–2582.

Herzog, S. [1986] The large scale structure in the near-wall region of turbulent pipe flow, PhD thesis, Cornell University.

Holmes, P., Lumley, J. L. and Berkooz, G. [1996] *Turbulence, Coherent Structures, Dynamical Systems and Symmetry* (Cambridge University Press).

Kim, J., Moin, P. and Moser, R. J. [1987] Turbulence statistics in a fully developed channel flow at low Reynolds number, *J. Fluid Mech.* **177**, 133–166.

Kirby, M. [2000] *Geometric Data Analysis*: *An Empirical Approach to Dimensionality Reduction and the Study of Patterns* (Wiley-Interscience).

Kulasiri, D. and Verwoerd, W. [2002] *Stochastic Dynamics; Modelling Solute Transport in Porous Media* (Elsevier, Amsterdam).

Lennon, J. M. [2004] Application of particle image velocity to the hydraulic jump, thesis for Master of engineering, Pennsylvania State University.

Liu, Z. C., Adrian, R. J. and Hanratty, T. J. [1994] Reynolds number similarity of orthogonal decomposition of the outer layer of turbulent wall flow, *Phys. Fluids* **6**(8), 2815–2819.

Liu, Z. C., Adrian, R. J. and Hanratty, T. J. [2001] Large-scale modes of turbulent channel flow: Transport and structure, *J. Fluid Mech.* **448**, 53–80.

MathsWorks, T. [2006] Matlab.

Moin, P. and Moser, R. D. [1989] Characteristic-eddy decomposition of turbulence in a channel, *J. Fluid Mech.* **200**, 471–509.

Moser, R. D., Kim, J. and Mansour, N. N. [1999] Direct numerical simulation of turbulent channel flow up to $Re_\tau = 590$, *Phys. Fluids* **11**(4), 943–945.

Nakagawa, H. I., Nezu, I. and Ueda, H. [1975] Turbulence in open channel flow over smooth and rough beds, *Proc. Japanese Society of Civil Engineers*, Vol. 241, pp. 155–168.

Nezu, I. and Nakagawa, H. [1993] *Turbulence in Open-Channel Flows* (IAHR-Monograph, Balkema).

Pope, S. B. [2000] *Turbulent Flows* (Cambridge University Press, United Kingdom).

Townsend, A. A. [1956] *The Structure of Turbulent Shear Flow* (Cambridge University Press, Cambridge).

Tursunov, A. A. [1969] Non-shock flows of water close to critical flow, *Proceedings of the All-Union Scientific Research Institute of Hydraulics*, Vol. 90, pp. 201–223.

VSN [2006] Genstat version 8.2.